ADVANCED ENERGY & SUSTAINABILITY RESEARCH
Open Access
www.advenergysustres.com

Synthesis and Electrochemical Performance of High-Entropy Spinel-Type Oxides Derived from Multimetallic Polymeric Precursors

Haotian Yang, Ge Chen, Jiaqi Ni, Sebastian Praetz, Delf Kober, Gabriel Cuello, Emiliano Dal Molin, Albert Gili, Christopher Schlesiger, Maged F. Bekheet, Dorian A. H. Hanaor, and Aleksander Gurlo**

High-entropy spinel-type oxides are synthesized by a modified Pechini process, wet chemistry approach, and solid-state synthesis method and characterized as anode materials for Li-ion batteries. The Pechini process that involves chelation and polyesterification reactions facilitates the formation of high-entropy spinel-type oxides without compositional segregation at ≈600 °C as confirmed by in situ and ex situ XRD. XAFS analysis and the Rietveld refinement of room-temperature neutron diffraction data suggest the composition ($Mn_{0.05}Fe_{0.48}Co_{0.47}$, tetrahedral)($Cr_{0.61}Mn_{0.52}Fe_{0.11}Co_{0.09}Ni_{0.68}$, octahedral)$O_4$ for phase-pure specimens. Compared to high-entropy spinel-type oxides synthesized by the solid-state method, the precursor-derived materials demonstrate higher specific capacity as anodes, in which the materials without citric acid addition exhibit low capacity fading at high current densities and maintained a capacity of ≈200 mAh g^{-1} after 1000 cycles. The generation of a rock-salt-type phase during cycling is confirmed for the first time by in situ charging–discharging XRD. The charging–discharging of this anode material is achieved mainly through the embedding–disembedding of lithium ions in the lattice of the generated rock-salt-type phase.

1. Introduction

In the ever-evolving landscape of energy storage solutions, researchers have been exploring innovative materials to improve the efficiency, safety, and sustainability of batteries. Although several developed metal-ion batteries, such as sodium ion,[1] potassium ion,[2] and magnesium ion,[3–5] lithium-ion batteries (LIBs) dominate the present battery market due to their high energy density, wide operation temperature range, rapid charge/discharge capability, and favorable cycling behavior.[6–11] Graphite is commonly used as the anode for most metal-ion batteries. However, the capacity of graphite is quite low to meet the high energy demand. Therefore, the development of alternative anode materials for metal-ion batteries has recently aroused great interest in research and technology.[3,4,10,11] Transition metal oxides with a spinel-type structure (space group of *Fd*-3 *m,* No. 227) have evoked considerable attention because of their attractive optical, magnetic, and electronic properties.[12,13] For instance, several spinel-type oxides such as Fe_3O_4,[14,15] Mn_3O_4,[16,17] and Co_3O_4[18–21] are regarded as potential anode materials because of their high theoretical capacities, which were generally 2–3 times that of commercial graphite (372 mAh g^{-1}).[22] Nevertheless, most transition metal oxides usually experience large volume changes during de-/lithiation, which results in electrode pulverization and rapid capacity fading.[23]

It has been reported that element doping could effectively enhance the structural stability and cycling performance of oxide

H. Yang, G. Chen, J. Ni, D. Kober, E. Dal Molin, M. F. Bekheet, D. A. H. Hanaor, A. Gurlo
Faculty III Process Sciences, Institute of Materials Science and Technology, Chair of Advanced Ceramic Materials
Technische Universität Berlin
Straße des 17. Juni 135, 10623 Berlin, Germany
E-mail: haotian.yang@ceramics.tu-berlin.de; gurlo@ceramics.tu-berlin.de

The ORCID identification number(s) for the author(s) of this article can be found under https://doi.org/10.1002/aesr.202400146.

DOI: 10.1002/aesr.202400146

S. Praetz, C. Schlesiger
Faculty II–Mathematics and Natural Sciences, Institute for Optics and Atomic Physics
Technische Universität Berlin
Straße des 17. Juni 135, 10623 Berlin, Germany

G. Cuello
Institut Laue-Langevin
71, av des Martyrs, BP 156 F-38042 Grenoble, France

A. Gili
Helmholtz-Zentrum Berlin für Materialien und Energie
14109 Berlin, Germany

electrodes.[13] In the dynamic realm of materials science, high-entropy ceramics have emerged as a fascinating and promising area of research. High-entropy ceramics consist of at least five randomly distributed metal cations alongside an anion sublattice.[24–26] These complex compounds, characterized by their unique crystal structures and diverse elemental compositions, have sparked immense interest due to their exceptional properties and wide-ranging applications.[27–30] High-entropy oxides of the composition $(Co_{0.2}Cu_{0.2}Mg_{0.2}Ni_{0.2}Zn_{0.2})O$ with a rock-salt structure have recently been employed as anode materials for LIBs, showing high specific capacities and excellent cycling performance, attributed to the entropy stabilizing effect during lithiation/delithiation.[22,31,32] However, the Mg in such HEOs is electrochemically inert, which may sacrifice the electrode capacity and reduce the energy density of the battery.[33]

In high-entropy binary ceramics, several cations are randomly distributed in the cationic sublattice.[34,35] For example, in high-entropy spinel-type oxides (HESOs), the cations randomly occupy tetrahedral and octahedral voids in the cubic close packing of oxygen anions.[36,37] The spinel-type structure offers unique opportunities as a multicomponent system due to its large and complex unit cell, which consists of 32-anion sites, surrounded by 24 cations organized in both octahedral and tetrahedral sites,[38] and allows the presence of cations in multiple oxidation states. In this way the spinel-type structure, allowing for variation of oxidation states of cations during charging and discharging, can enhance the specific capacity of the electrode material.[39] The crystal structures, oxidation states, and atomic occupancies will affect the electrical storage properties of HESOs. Depending on the distribution of cations over tetrahedral and octahedral sites, normal spinel, inverse spinel, and mixed spinel can be distinguished. To complicate matters further, the transition metal elements in HESOs usually exhibit multiple oxidation states, which makes the determination of the structure even more challenging.[27,40,41]

Since the first work on the electrochemical performance of a high-entropy spinel oxide, $(Cr_{0.2}Mn_{0.2}Fe_{0.2}Co_{0.2}Ni_{0.2})_3O_4$, with five electrochemically active elements,[42] numerous studies have emerged on using high-entropy spinel oxides as electrode materials.[43–47] However, the capacity and cycling performance of HESO prepared by conventional methods is still insufficient,[33,39] hindering its further development. Constructing different nanostructures for electrode materials is an efficient strategy to solve the mentioned problems and enhance the electrochemical performance due to the shortened Li^+ transport path, increased specific surface area, and increased number of active sites.[48,49] The chelation-polymerization synthesis route, also known as the Pechini process, is known to be conducive to the formation of single phases for compositions with multiple cation species, at lower temperatures than would otherwise be possible.[50–52] This is particularly useful for the processing of ternary or quaternary transition metal oxides.

Recently, we developed a modified Pechini process for the synthesis of high-entropy carbides,[53] in which the introduction of a chelating agent homogenizes the distribution of metal ions in the liquid precursor at the molecular level which in turn lowers the formation temperature of the high-entropy materials in the subsequent thermal treatment step. In this work, we apply our molecular precursor-based approach to synthesize high-entropy spinel-type oxides and investigate their electrochemical performance as anodes for LIBs.

2. Results and Discussion

2.1. Structure and Decomposition Mechanism of Multimetallic Polymeric Precursors to High-Entropy Spinel-Type Oxides

High-entropy spinel-type oxides were synthesized by the modified Pechini method reported previously,[53] and compared to those obtained by the conventional solid-phase synthesis (SSM). The effect of a chelating agent (i.e., citric acid) on the formation and morphology of high-entropy materials was also investigated by comparing samples synthesized with (i.e., by Pechini method) and without (i.e., by wet chemistry approach) citric acid. **Table 1** gives an overview of the samples investigated in this work. The abbreviations used for the samples in this work consist of the designation of the synthesis method (SSM or PD) and the temperature of the heat treatment (600, 700, 800, and 1000 °C); the multimetallic polymeric precursors are designated by the letters -PR.

The structure of multimetal polymeric precursors PD0-PR and PD5-PR was examined by FTIR. Pure citric acid and ethylene glycol were also measured for comparison. As displayed in **Figure 1**a, the adsorption bands at 1080 and 1030 cm^{-1} can be attributed to the C-O stretching vibration of ethylene glycol. The bands from 880 to 860 cm^{-1} are attributed to the C-H deformation vibrations. The strong bands at 1740 and 1696 cm^{-1} are attributed to the C═O stretching vibration of carboxylic groups in citric acid.[62] The absorbance bands at 1620 cm^{-1} observed in the spectra of polymer precursors can be assigned to the H—O—H scissor bending vibration of water.[63] The absorbance band at 1450 cm^{-1} corresponds to the deformation vibration of C—H. The absorbance band at 1200 cm^{-1} is attributed to the C—O stretching vibration of the ester group. The bands at around 665 and 640 cm^{-1} observed in the spectra of multimetal polymers are attributed to stretching of Me—O in the Me—O—C chain,[64,65] which were not observed in pure ethylene glycol. The bands of C═O stretching vibration (1720 and 1634 cm^{-1}) in PD5-PR exhibited a red shift compared to those of citric acid, suggesting the chelation of metal cations.

Table 1. Synthesis parameters and abbreviations of the specimens studied in this work.

Synthesis method	Citric acid [mol%]	Precursor	Heat treatment at 600 °C	Heat treatment at 700 °C	Heat treatment at 800 °C	Heat treatment at 1000 °C
Solid state	–	–	SSM-600	SSM-700	SSM-800	SSM-1000
Wet chemistry	0	PD0-PR	PD0-600	PD0-700	PD0-800	PD0-1000
Modified Pechini	50	PD5-PR	PD5-600	PD5-700	PD5-800	PD5-1000

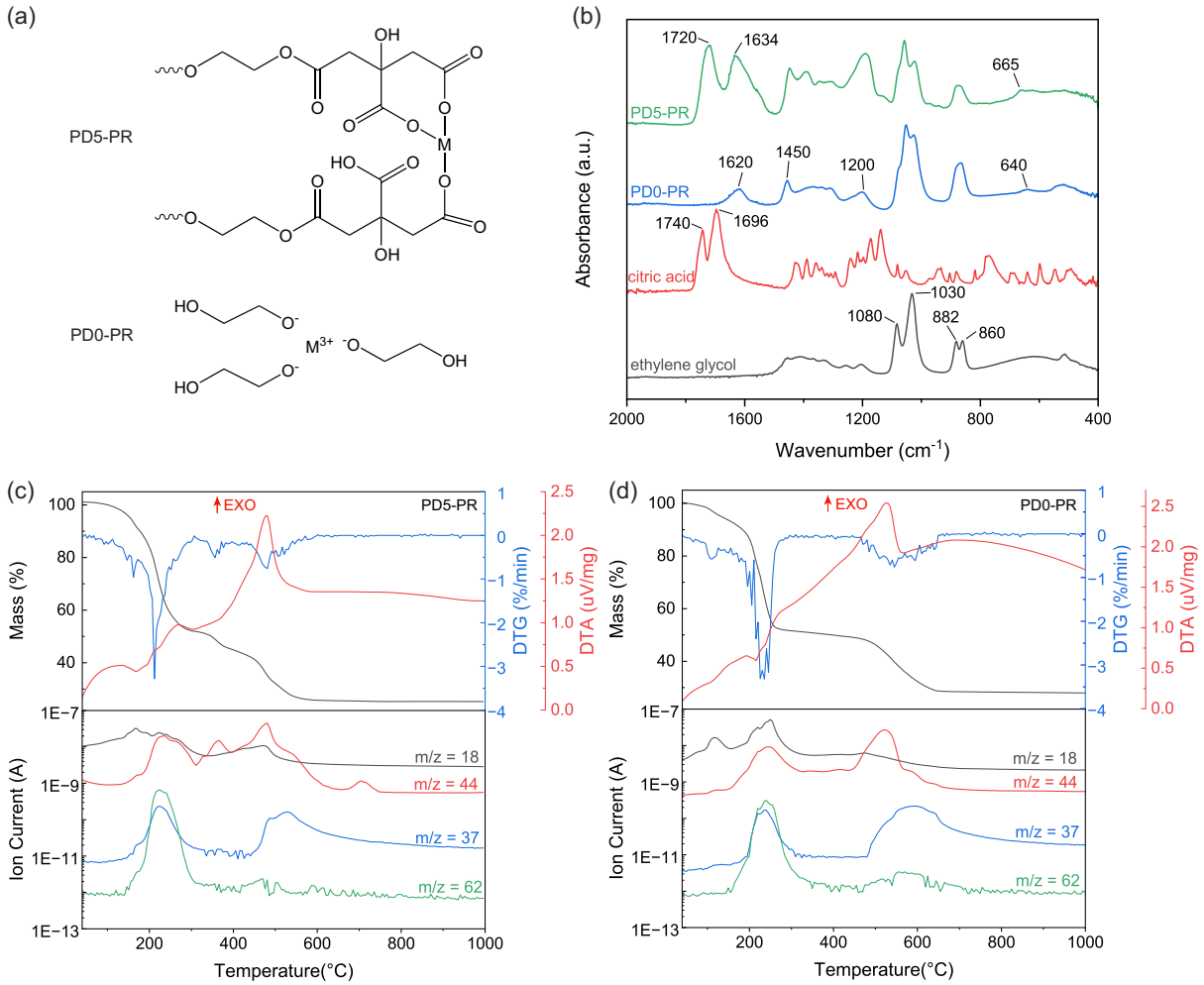

Figure 1. a) Possible molecular structure of the PD0-PR and PD5-PR precursors with M^{3+} cations taken as an example and ethylene glycol. b) FTIR spectra of ethylene glycol, citric acid, and multimetal polymers. Results of simultaneous thermal analysis coupled with mass spectrometry for c) PD5-PR and d) PD0-PR, respectively.

As shown in Figure 1c,d, a significant mass loss of about ≈50% is accompanied by an endothermic peak at about 200 °C, which corresponds to the thermal decomposition of polymeric precursors and the evaporation of ethylene glycol (m/z = 62), H_2O (m/z = 18), and HCl (m/z = 37). The main difference between the two samples was observed in the temperature range of 230–440 °C, where the sample PD0-PR had a plateau with a nearly constant slope and almost zero mass loss, while the sample PD5-PR had multiple inflection points correlated with peaks in mass spectrometry, which are attributed to the multistep decomposition of the formed polymers accompanied by the release of CO_2 (m/z = 44). When the temperature is raised to 500 °C, a further mass loss of about ≈15% is observed, accompanied by a large amount of CO_2 releasing, which suggests the exothermic oxidation of the residual carbon. No weight change is observed above 650 °C, indicating the end of the thermal decomposition of the polymeric precursors with a yield of around 20–30 wt%.

2.2. Composition, Structure, and Morphology of High-Entropy Spinel-Type Oxides

As shown in **Figure 2**a, the X-ray diffraction (XRD) pattern of the SSM-600 sample with a diffuse scattering background displays XRD reflections of starting binary oxides used in the synthesis, indicating that crystalline spinel-type oxide is not formed at this temperature. After heating to 700 °C, the XRD reflections of the spinel-type oxide dominate, while the reflections of the starting binary oxide phases disappear, with the exception of the reflections of the Mn_2O_3 phase, which remains as a minor impurity. When the temperature is further increased to 800 °C, only the XRD reflections of the cubic spinel-type structure are observed, indicating that the formation of phase-pure high-entropy spinel-type oxide is completed.

In contrast, the homogeneous distribution of the cations at the molecular level in the PD5 specimens facilitates the formation of a high-entropy spinel-type oxide at a lower heat treatment

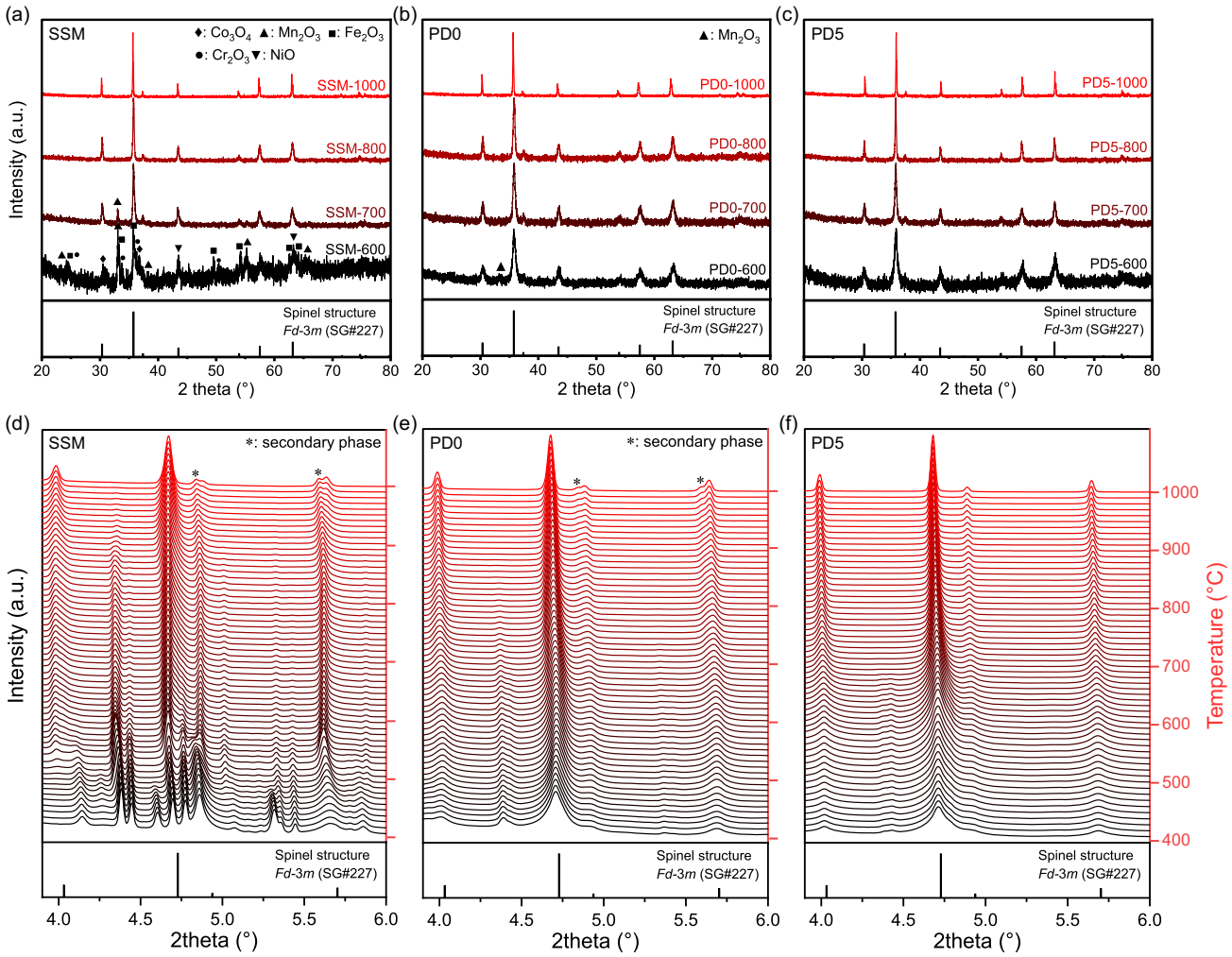

Figure 2. a–c) The ex situ XRD patterns collected at $\lambda = 1.5406$ Å of samples synthesized by a) SSM and derived from b) PD0-PR and c) PD5-PR and heat treated at different temperatures for 1 h. d–f) The high-temperature in situ XRD patterns collected at $\lambda = 0.2073$ Å from 400 to 1000 °C of samples synthesized by d) SSM and derived from e) PD0-PR and f) PD5-PR; all samples were preheat treated at 400 °C; the temperature difference between each two adjacent patterns is 10 °C. The benchmark Bragg position was calculated by the Rietveld refinement based on the high-resolution synchrotron XRD data ($\lambda = 0.2073$ Å) of PD5-1000 (Figure S1, Supporting Information).

temperature of about ≈600 °C (Figure 2c). A minor Mn_2O_3 phase can still be observed in the sample PD0-600 (Figure 2b) and then disappeared at higher calcination temperatures. The spinel-type high-entropy oxide synthesized by all three methods was found to be stable, and no phase transformation occurred when the temperature was increased to 1000 °C, while the XRD reflections became narrower due to the increase in the crystallite size of the specimen. This increase in the crystallite size of the spinel with increasing calcination temperature is consistent with the results of scanning electron microscopy (SEM), which shows an increase in the particle size of the samples with temperature (**Figure 3**).

Nanosized spinel-type oxide in already formed the polymeric precursors PD0-PR and PD5-PR heated to 400 °C as indicated by broad reflections in the corresponding XRD patterns (Figure 2e, f) confirming again the advantage of compositional homogeneity in the precursors for the formation of high-entropy materials, which is consistent with our previous study on high-entropy carbides.[53] For all the synthesis methods, the reflections of the binary oxides (either starting materials or side phases) in all samples gradually disappear with increasing temperature. Due to the high heating rate and the absence of a dwell step, the phase transition is hysteresis with temperature during in situ XRD measurement. In the SSM and PD0 samples, the reflections at 4.83 and 5.59° still exist up to 1000 °C, which can be attributed to the secondary phases of solid solutions with elemental segregation similar to what was observed in our previous study.[53] PD5 sample transforms to a single-phase high-entropy spinel-type oxide already below 700 °C, and its crystallinity and crystallite size increase with increasing temperature. The formation of high-entropy materials at such low temperature, which is reported here for the first time, is due to the higher initial homogeneity and the shorter diffusion distance for cations achieved by cation chelation. By introducing citric acid, each metal ion in the

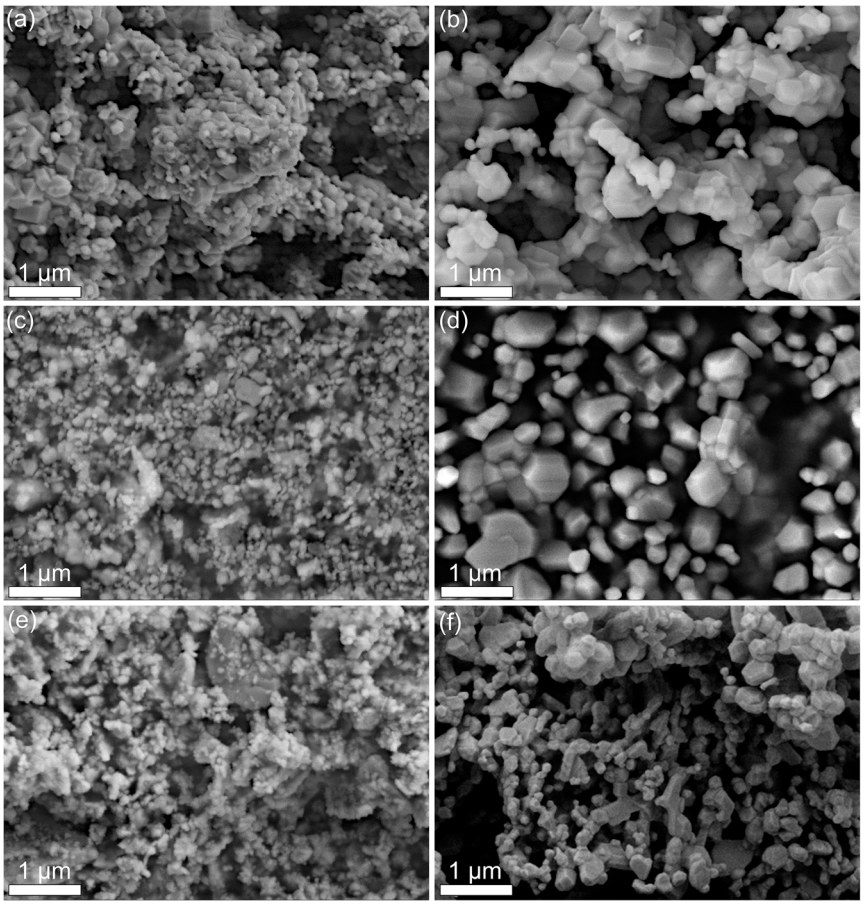

Figure 3. SEM images of a) SSM-800, b) SSM-1000, c) PD5-800, d) PD5-1000, e) PD0-800, and f) PD0-1000 at 20 k magnification.

liquid precursor was chelated by the multidentate ligand, preventing aggregation of the cations and segregation of the components, resulting in steric confinement and homogeneous distribution of the cations. The chemical homogeneity maintained in the specimen shortens the diffusion distance of the atoms during calcination and thus significantly reduces the temperature required for the formation of high-entropy ceramics.

The oxidation states of the cations and the site occupancies in the spinel-type structure were characterized by X-ray absorption fine structure (XAFS) analysis. Despite the Ni-K edge spectrum of PD5-800 shows some differences with that of $NiFe_2O_4$ in the X-ray absorption near edge structure (XANES) region (**Figure 4**a) due to lower energy resolving power with the laboratory, it is similar to those of $NiFe_2O_4$ and NiO, suggesting that the Ni in the sample is in the oxidation state of 2+ and the octahedral sites considering the Ni^{2+} coordination environment in NiO and $NiFe_2O_4$. The Fourier transformed extended X-ray-absorption fine-structure (FT-EXAFS) of the Ni (Figure 4b) demonstrates similar a local environment of PD5-800 with that of $NiFe_2O_4$, which further confirms octahedral occupancy in PD5-800. Similarly, the Fe-K edge spectrum and the FT-EXAFS of Fe in PD5-800 show great agreement with that of $NiFe_2O_4$ (Figure 4c,d), which suggests that the Fe in the sample is in a 3+ state and both octahedral and tetrahedral sites considering the iron coordination environment in $NiFe_2O_4$. A small pre-edge peak and the FT-EXAFS spectrum support this inference. However, the ratio of Fe occupancy in octahedral and tetrahedral sites still needs further investigation. The Cr-K edge position of PD5-800 is in good matching the Cr_2O_3 and $CuCr_2O_4$ (Figure 4f) which suggests octahedral coordination of Cr^{3+}. The pre-edge missing visible in the entrance of Figure 4e also indicates that most of the Cr^{3+} is in octahedral sites. The Mn-K edge position of PD5-800 is located between Mn_2O_3 and MnO_2 (Figure 4g), implying a mixed oxidation state of 3+ and 4+. Linear combination fitting (LCF) of sample spectra with the reference spectra of Mn_2O_3 and MnO_2 has been applied to the XANES range, and the ratio of Mn^{3+}: Mn^{4+} is calculated to be ≈48.9: 51.1. However, the lack of suitable reference materials to perform LCF resulted in considerable fitting deviations (Figure S4, Supporting Information). The oxidation state of Mn in PD5-800 requires further investigation, and the same holds for the Mn-coordination. The Co-K edge of the PD5-800 is at the same position as CoO as well as close to $CoFe_2O_4$ (Figure 4i), which indicates that Co^{2+} is a dominant oxidation state in the sample. A small shoulder before the edge at around 7705 eV indicates a small pre-edge feature, which suggests a partially tetrahedral coordination of

cobalt cations; however, the fraction of octahedrally/tetrahedrally coordinated cobalt cannot be estimated due to mismatch with reference materials (Figure 4j).

To further study the crystal structure and the site occupancies of the high-entropy spinel-type oxide, Rietveld refinement based on the neutron diffraction data was performed. The neutron diffraction was chosen due to the significant differences in the scattering intensities of different cations. To minimize the error during the refinement, the occupation factor of each cation was set according to the inductively coupled plasma optical emission spectroscopy (ICP-OES) results (Table S1, Supporting Information), and the occupation factors of tetrahedral and octahedral sites were constrained to be 1 and 2, respectively. The Ni and Cr were both constrained to occupy the octahedral sites

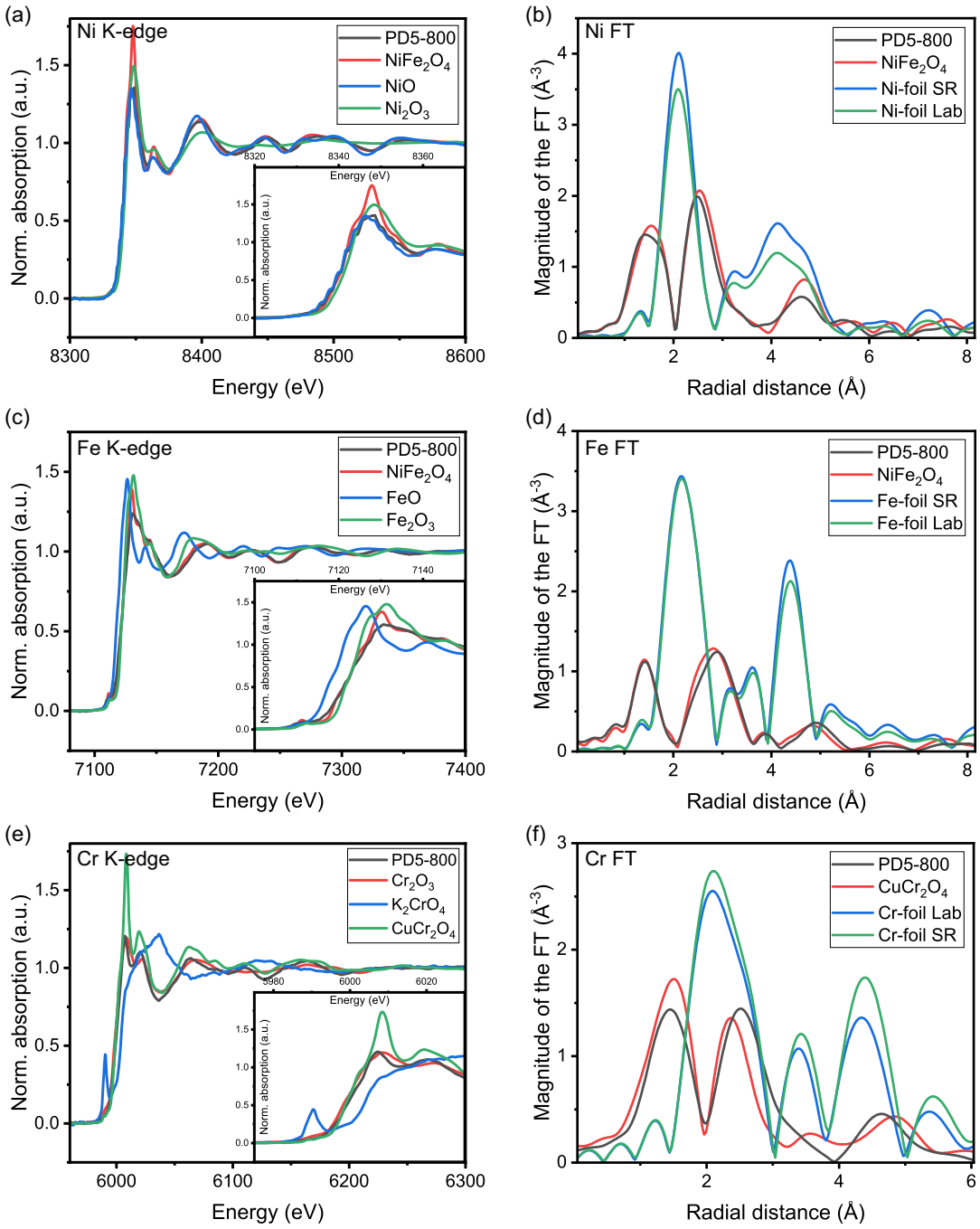

Figure 4. The normalized XAFS and XANES spectra of a) Ni K-, c) Fe K-, e) Cr K-, g) Mn K-, and i) Co K-edge of PD5-800. The magnitude of the Fourier transform of the EXAFS spectra of b) Ni, d) Fe, f) Cr, h) Mn, and j) Co, respectively. The data of the metal foils and powder measured in our laboratory (marked as Lab) and from SPring-8 (marked as SR) was used for calibration.

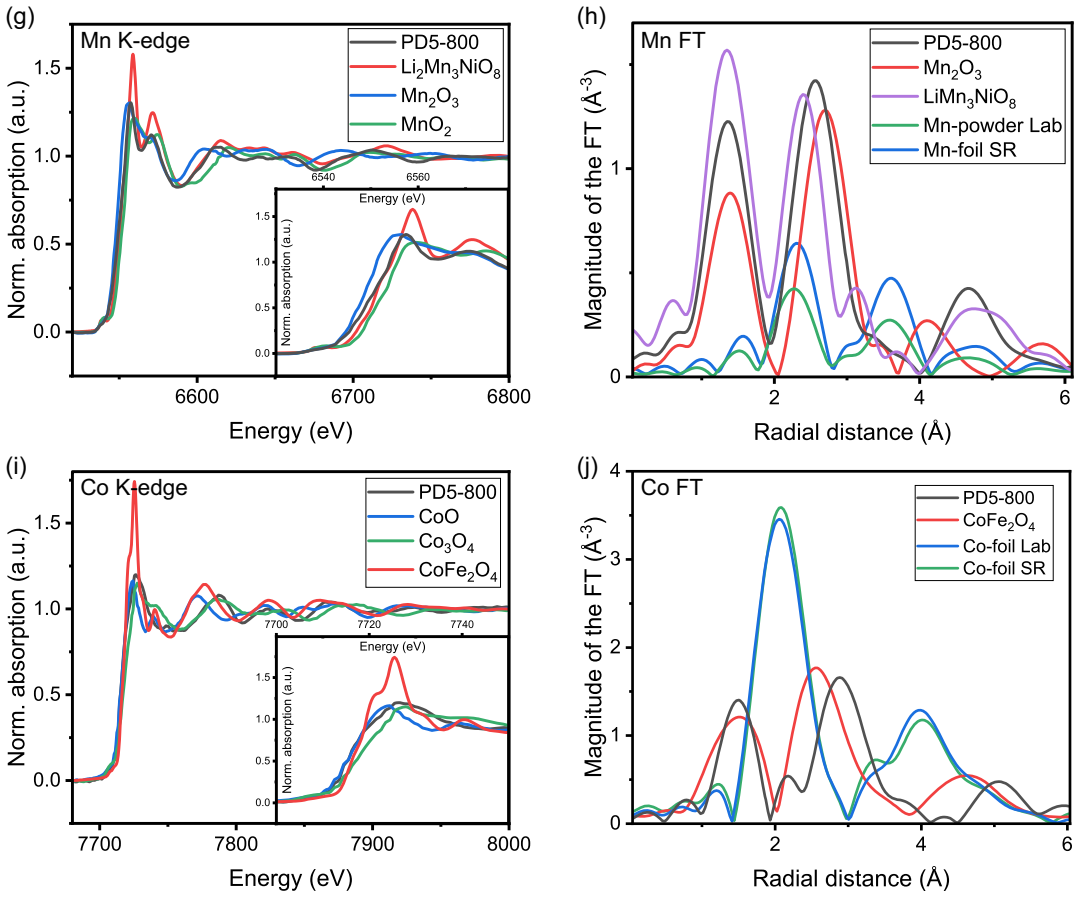

Figure 4. Continued.

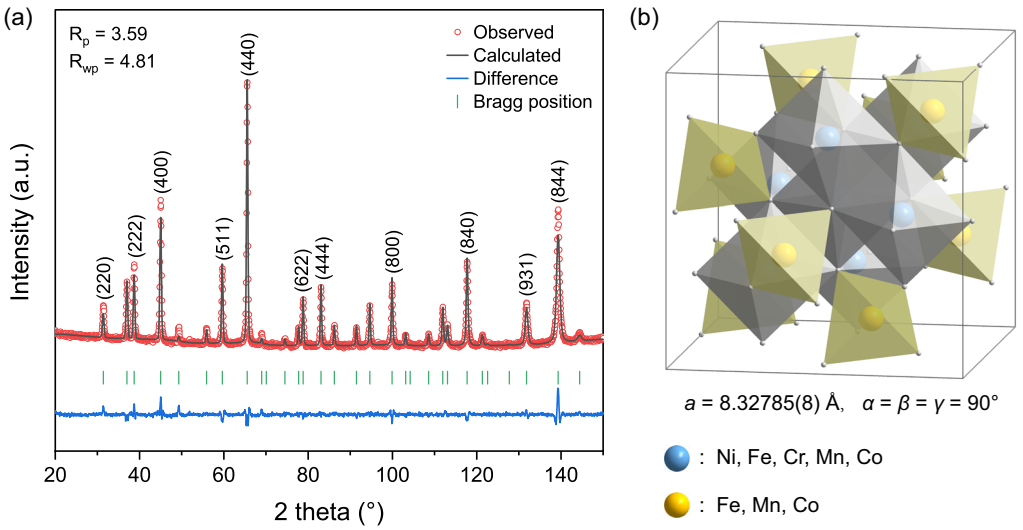

Figure 5. a) Rietveld refinement based on the neutron diffraction data ($\lambda = 1.5940$ Å) of PD5-800. b) The crystal structure of the synthesized spinel-type high-entropy oxide. The yellow spheres represent the atoms in tetrahedral sites and the blue spheres represent the atoms in octahedral sites in the spinel-type structure. The gray spheres represent oxygen.

based on the XAFS results. The Rietveld refinement was performed on the neutron diffraction data of PD5-800, and the occupation factors of Fe, Co, and Mn were refined (**Figure 5**). It is determined that the Mn prefers the octahedral sites and only a small amount of Mn occupies the tetrahedral sites, while reversely the Co prefers the tetrahedral sites. The lattice

Table 2. Structural parameters Space Group *Fd*-3 *m* (No. 227)[a] of the specimen from Rietveld refinement of the neutron diffraction data collected on the PD5-800 specimen.

Atoms	Wyckoff position	x[b]	y[b]	z[b]	Biso(Å^2)[c]	Occupation factor
Cr (t)[d]	8a	0.12500	0.12500	0.12500	0.839 (62)	–
Mn (t)[d]						0.053 (20)
Fe (t)[d]						0.482 (18)
Co (t)[d]						0.465 (39)
Ni (t)[d]						–
Cr (o)[e]	16 d	0.50000	0.50000	0.50000	0.309 (41)	0.610
Mn (o)[e]						0.516 (20)
Fe (o)[e]						0.109 (18)
Co (o)[e]						0.090 (39)
Ni (o)[e]						0.675
O	32e	0.25967 (8)	0.25967 (8)	0.25967 (8)	0.616 (23)	4

[a] $R_p = 3.59\%$, $R_{wp} = 4.81\%$, $R_f = 2.73\%$, and $R_B = 4.24\%$. [b] Fractional atomic coordinates. [c] Isotropic temperature factors. [d] The atoms in the tetrahedral site. [e] The atoms in the octahedral site.

parameters and the atomic occupancies of PD-5 are shown in **Table 2**. The crystal structure and lattice parameters of PD5-800 were further confirmed by transmission electron microscopy (TEM). The diffraction rings of polycrystalline PD5-800 in the selected area electron diffraction (SAED) pattern (**Figure 6**b) correspond to the (111), (220), (311), and (222) lattice planes of the cubic spinel structure, and the interplanar distance (Figure 6c) measured by the high-resolution transmission electron microscopy (HR-TEM) consists well with the interplanar distance of (111) lattice plane determined by Rietveld refinement based on the high-resolution synchrotron XRD (Figure S1–S3, Supporting Information). Energy-dispersive X-ray spectroscopy (EDS) mapping confirmed the uniform distribution of cations in PD5-800 (Figure 6d), consistent with the formation of homogeneous spine-type high-entropy oxides. The TEM images, SAED, and EDS results of PD0-800 and SSM-800 are provided in the Supporting Information (Figure S12, S13, Supporting Information).

Table 3 summarizes the composition as well as the oxidation state and coordination of metal cations (i.e., occupancy of tetrahedral and octahedral sites in the spinel-type structure) of the PD5-800 specimens from the results of ICP-OES, EDS, XAFS characterizations, and Rietveld refinement of neutron diffraction. The ICP-OES and EDS data confirm the stoichiometry targeted in the synthesis (with a very slight deviation). Based on the ICP-OES results, the composition of the PD5-800 specimens can be given as $(Cr_{0.20}Mn_{0.19}Fe_{0.20}Co_{0.19}Ni_{0.22})_3O_4$. Additional information about the oxidation state and coordination of metal cations is provided by XAFS, as described above. Both cations Ni^{2+} and Cr^{3+} occupy the octahedral sites of the spinel-type structure, while Fe^{3+} is distributed in both octahedral and tetrahedral sites. The XAFS results suggest the following formula that considers the oxidation states of the cations: $(Cr^{3+}_{0.20}Mn^{3+}_{0.093}Mn^{4+}_{0.097}Fe^{3+}_{0.20}Co^{2+}_{0.19}Ni^{2+}_{0.22})_3O_4$. Rietveld refinement of the neutron diffraction data suggests both tetrahedral and octahedral sites for manganese-cations (i.e., Mn^{3+} and Mn^{4+}) and Co^{2+}. On the basis of all that data, the chemical formula of PD5-800 can be given as ($Mn_{0.05}Fe_{0.48}Co_{0.47}$, tetrahedral)($Cr_{0.61}Mn_{0.52}Fe_{0.11}Co_{0.09}Ni_{0.68}$, octahedral)$O_4$. In this formula, we do not consider the oxidation states of the cations since reliable information was not obtained for all of them.

2.3. Electrochemical Performance as Anodes in Lithium-Ion Batteries

The initial charge/discharge curves of the HESO anode at the current density of 37 mA g^{-1} are shown in **Figure 7**a. With the exception of SSM-1000, all other specimens showed an initial capacity higher than 1000 mAh g^{-1}, which demonstrates the potential of this spinel-type high-entropy oxide as a high-capacity anode for LIBs. During the discharge process, it's obvious that all 6 HESO batteries have a clear plateau voltage at around 0.75 V, which represents the reduction of metal oxide and the formation of a solid-electrolyte interphase (SEI) layer, verified in literature.[33,39] It can be observed that the batteries with polymer precursor-derived materials have higher initial capacities than the solid-state synthesized anodes. What's more, the capacities of all materials calcined at 800 °C are higher than those of the corresponding materials calcined at 1000 °C. This can be attributed to the smaller grain size resulting from polymer-derived methods and lower calcination temperatures (Figure 3), which endows higher specific surface area and active sites. At the first charge, the capacities of all the samples were reduced and their Coulombic efficiency was about 70% (**Table 4**). The large initial irreversible capacity and low initial Coulombic efficiency can be attributed to the irreversible reactions of anode materials (e.g., irreversible structural and morphology changes) and the inevitable formation of the SEI layer on the electrode surface. In addition, the charge curves showed a fast voltage increase when the voltage exceeded 2 V, which was due to the over-potential at >2 V, leading to a significant voltage drop to 2.3 V after charging.

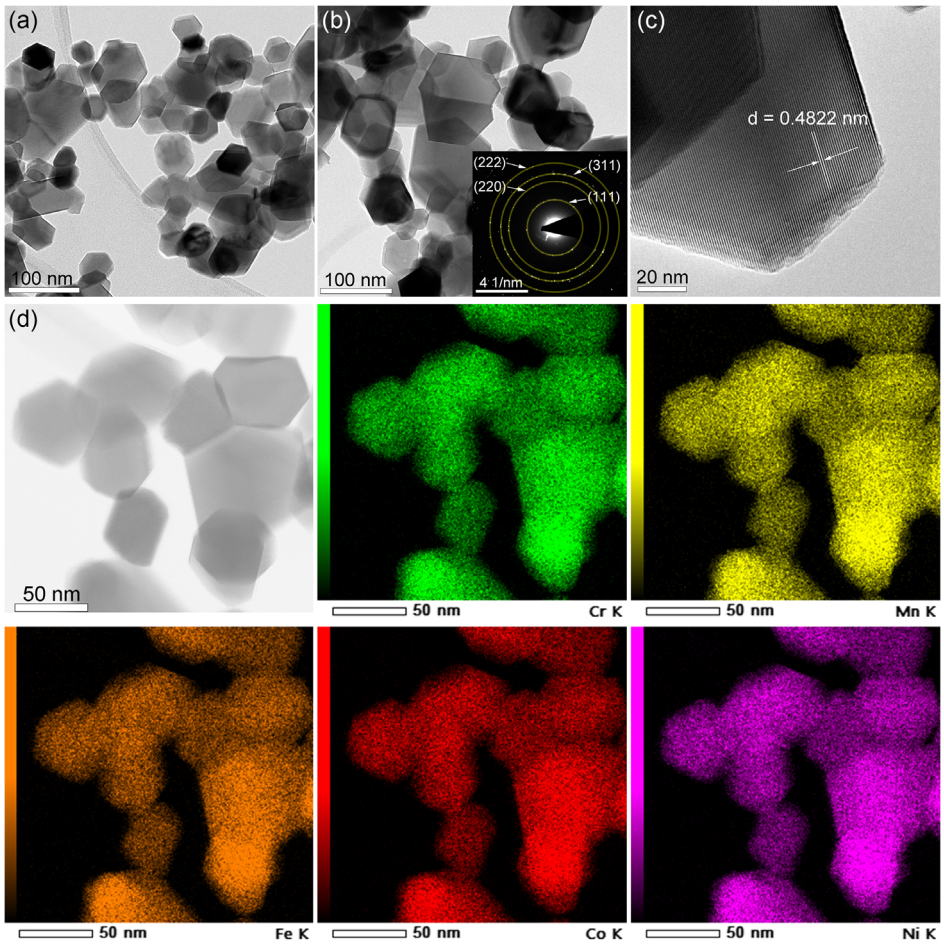

Figure 6. TEM images of PD5-800. a–c) Brightfield TEM images of the dispersed PD5-800 grains. A SAED pattern of polycrystalline PD5-800 was inserted in (b). c) HR-TEM image of PD5-800 grains. d) EDS mappings of Cr, Mn, Fe, Co, and Ni in PD5-800.

Table 3. Composition, oxidation states, and coordination of metal cations in the sample PD5-800.

Cation	Cationic fraction [at%]						
	Targeted	ICP-OES	EDS	XAFS		Neutron diffraction	
Cr	20	20.34 (80)	16.52 (26)	Cr^{3+}	20	Cr (t)	–
						Cr (o)	20.34
Mn	20	18.95 (8)	19.32 (46)	Mn^{3+}	9.27 (15)	Mn (t)	1.77 (66)
				Mn^{4+}	9.68 (23)	Mn (o)	17.2 (66)
Fe	20	19.72 (28)	20.19 (50)	Fe^{3+}	20	Fe (t)	16.07 (60)
						Fe (o)	3.63 (60)
Co	20	18.51 (39)	21.74 (34)	Co^{2+}	20	Co (t)	15.5 (13)
						Co (o)	3.0 (13)
Ni	20	22.49 (40)	22.23 (21)	Ni^{2+}	20	Ni (t)	–
						Ni (o)	22.49

The rate performance of HESO electrodes from different processes was measured under different current densities, as shown in Figure 7b,c. Here, the batteries with polymer precursor-derived materials showed excellent capacity (around 800 mAh g^{-1}) at a low current density of 74 mA g^{-1}, while the capacities of solid-state synthesized anode are much lower, around 500–600 mAh g^{-1}. The capacities of materials calcined at 1000 °C are slightly lower than those calcined at 800 °C (Figure 7b), and its capacity fading is more significant at high current density. The similar and clear potential plateaus reveal the stable and superior rate properties. The capacities of PD0-800 in this work are compared with those reported for binary, ternary, quaternary, and high-entropy spinel-type oxide particles at low current densities (60–100 mA g^{-1}).[15,16,47,66–73] The capacity of PD0-800 at 74 mA g^{-1} is comparable to other high-entropy spinel oxides and higher than most medium-entropy and low-entropy spinel oxides (**Figure 8**). Overall, as the number of cations increases, the capacities of spinel oxides as anodes for LIBs gradually increase, which can be attributed to the synergistic effect of multiple metal cations with different reaction potentials and variable valence states in high-entropy ceramics.

With the increasing current density, the capacity of all the samples decreased gradually due to the kinetic limitations of diffusion-driven lithiation/delithiation.[31,74] The polymer precursor-derived materials showed excellent high-rate performance

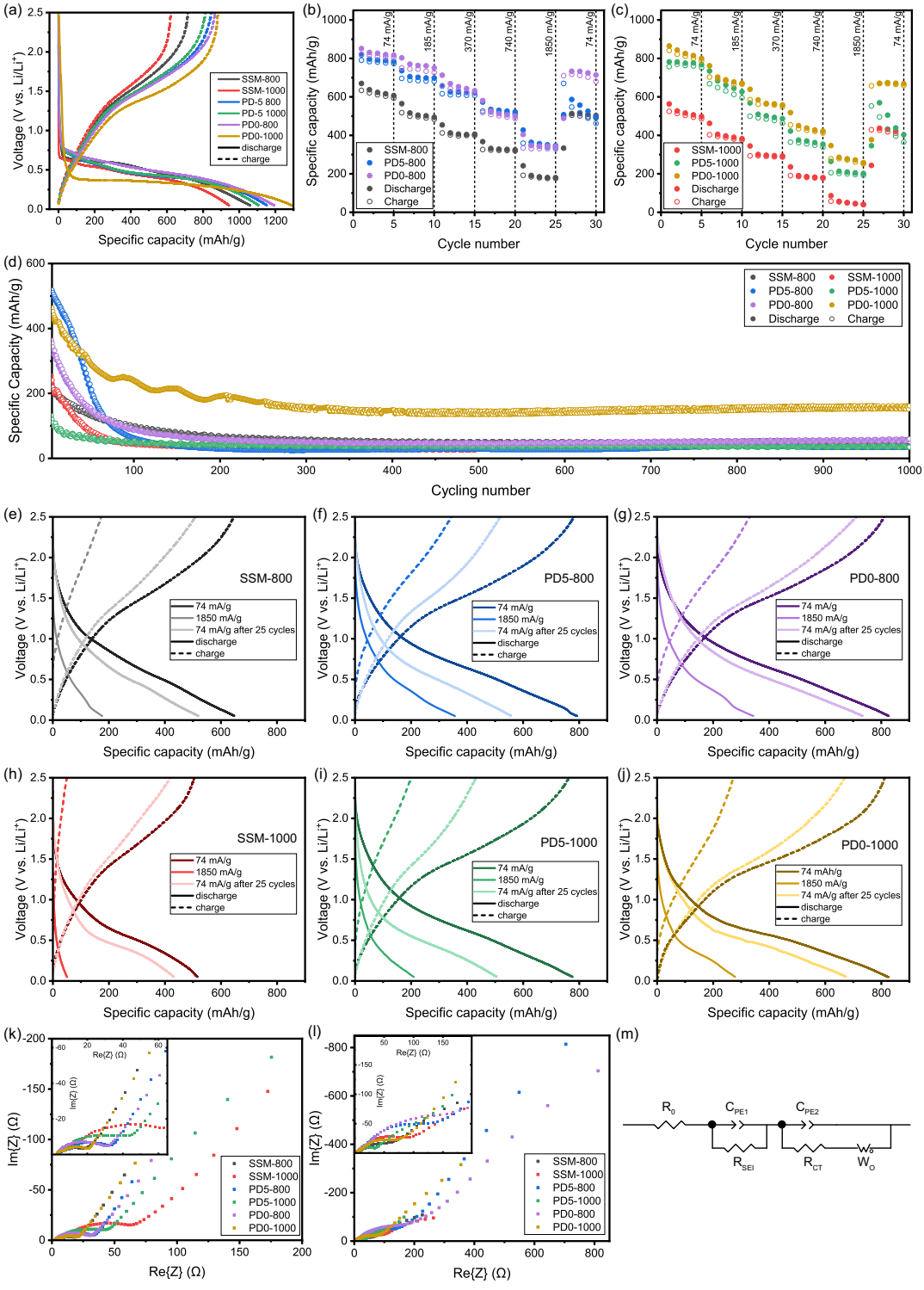

Figure 7. Electrochemical performance of the synthesized spinel-type high-entropy oxides as anodes for LIBs: a) Voltage versus capacity profiles of the first cycle at a current density of 37 mA g^{-1}. b,c) The rate performance of cells with 800 °C and 1000 °C calcined HESO. d) The cycle performance at a specific current of 1 A g^{-1} for 1000 cycles. e–j) Voltage versus capacity profiles at different current densities. Data were selected from the third cycle of each current density. Nyquist plots and their partial magnification of cells with different active materials k) after 10 cycles and l) after 1000 cycles at a current density of 500 mA g^{-1}. Data discharged to 50% state of charge were selected for electrochemical impedance spectroscopy (EIS). m) The equivalent circuit used to fit the EIS data.

Table 4. Specific capacities and corresponding Coulomb efficiencies of the first cycle.

Sample IDs	C_{charge} [mAh g^{-1}][a)]	$C_{discharge}$ [mAh g^{-1}][b)]	Coulombic efficiency at first cycle [%]	Capacity fading after 25 cycles [%][c)]
SSM-800	1060.18	715.48	67.49	17.72
SSM-1000	943.15	620.69	65.81	16.31
PD5-800	1152.63	845.14	73.32	29.62
PD5-1000	1106.94	813.13	73.46	34.88
PD0-800	1193.69	866.52	72.59	11.33
PD0-1000	1290.87	882.53	68.37	18.37

[a)]Specific capacity of the first charge. [b)]Specific capacity of the first discharge. [c)]Calculated from the capacities at 74 mA g^{-1} after 25 cycles and the capacities at the initial 74 mA g^{-1}, and the values of the third cycles of discharge were used.

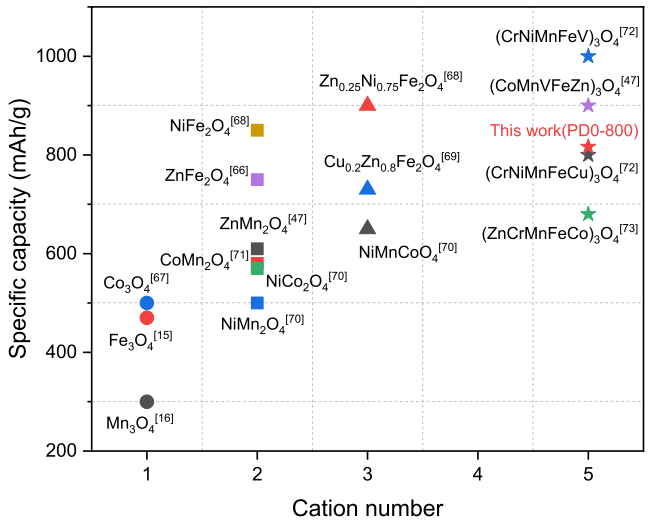

Figure 8. The reported specific capacities at low current densities (60–100 mA g^{-1}) of binary, ternary, quaternary, and high-entropy spinel-type oxides as anodes in LIBs. Data from refs. [15,16,47,66–73].

when the current density reached 1850 mA g^{-1}. The capacity of PD5-800 is 356.64 mAh g^{-1}, which is about 2 times that of SSM-800 (184.49 mAh g^{-1}) and 7 times that of SSM-1000 (50.62 mAh g^{-1}) at 1850 mA g^{-1}. The plateau part also decreased significantly with increasing current density in the voltage versus capacity profiles. As shown in Figure 7h, the plateau segment of SSM-1000 at 1850 mA g^{-1} almost disappeared, suggesting few reactions took place at high current density. The plateau segment could still be observed in the polymer-derived electrodes (Figure 7f,g,i,j), indicating the smaller grain size with higher specific surface facilities and the reactivity of anode material during fast charging/discharging. Meanwhile, overpotential increased at high current density, as the voltage increased significantly above 1.5 V without much increase in capacity and dropped fast during rest time (6 s in this work) after charging. When the 25 cycles of rate test ended and the current density returned to 74 mA g^{-1}, all six HESO batteries showed obvious capacity fading. The materials with the addition of citric acid have the most serious capacity fading, with 29.62 and 34.88% loss for PD5-800 and PD5-1000, respectively. Even worse, the capacity continued to decline with increasing cycles. In contrast, the polymer precursor-derived materials without the addition of citric acid demonstrate optimum stability. PD0-800 was able to return to and stabilize its capacity at about 733.11 mAh g^{-1} after 25 cycles, and the capacity fading is only 11.33%, which is due to the fact that the diffusion properties of active materials are greatly affected after high current density charging and discharging, which will be discussed in detail in the Nyquist plots.

The cycling performance of the cells with different electrode materials for 1000 cycles at a current density of 1 A g^{-1} is shown in Figure 8d. In the first 100 cycles, the capacities of all the samples decreased gradually, with the fastest decrease occurring for PD5-800 and the slowest for PD0-1000, which is consistent with the observed capacity fading (Table 4). After 100 cycles, the capacities of most samples declined to levels below 100 mAh g^{-1} and subsequently reached a state of stabilization. The capacity fading can be attributed to changes in the morphology of the active material during repeated charging and discharging at high currents, which has been observed through SEM of electrodes featuring active material. A comparative examination of the PD0-derived electrode materials (**Figure 9**a,b) reveals distinctions when contrasted with the PD5-derived electrode (Figure 9c,d). Before cycling, distinctly large grains of ≈200 and ≈500 nm were observed for the active materials of PD0-1000 and PD5-1000, respectively. After 1000 cycles, the grains of PD0-1000 were fragmented to tens of nanometers in diameter, while the grains of PD5-1000 were fragmented to a scale difficult to observe by SEM. Large grains of active material, which are dispersed on a network of carbon black in electrodes, broke up after 1000 cycles, producing agglomerated small particles that hinder the contact of active material with the carbon black network, resulting in poorer conductivity. What is more, the huge specific surface area and the large number of defects of the produced small particles trigger many side reactions; thereby, these two factors lead to a significant capacity fading of PD5-1000. The capacity of the PD0-1000, on the other hand, stabilized after 200 cycles and still reached about 200 mAh g^{-1} after 1000 cycles (Figure 8d). The cycling curve of PD0-1000 showed several ups and downs at 80–200 cycles, which can be attributed to the repeated generation and destruction of the SEI layer.

As shown in Figure 7k, after 10 cycles, all the samples exhibited similar diffusion phenomena and approximately similar internal resistances (≈3 Ω). However, SSM-1000 showed the highest charge transfer resistance (with the biggest semicircle diameter of ≈80 Ω), followed by PD5-1000 and PD5-800. In contrast, PD0-1000 and SSM-800 (≈20 Ω) exhibited the lowest charge transfer resistance and SEI resistance (≈6 Ω), corresponding to the shortest reaction relaxation time. After 1000 cycles, PD0-800 and PD0-1000 components maintained stable diffusion resistance. However, SSM-1000 and PD5-1000 exhibited a significant decrease in diffusion coefficients (reduced diffusion slopes). At this point, the high-current discharge performance of the electrodes was weaker, indicating poor high-rate performance, as also confirmed by Figure 7c. Additionally, after long-term cycling at high current densities, the charge transfer resistance of the electrodes increased in all batteries, prolonging

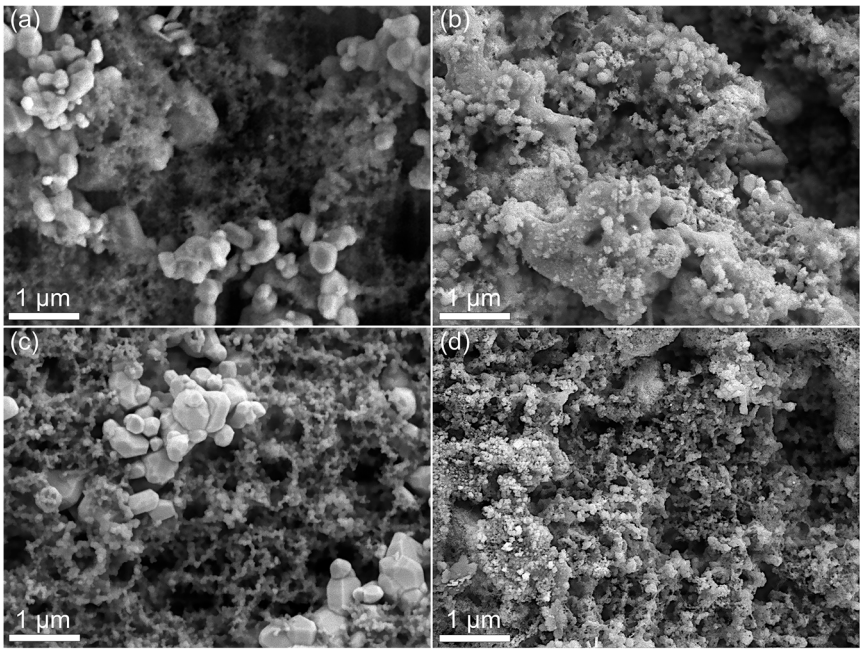

Figure 9. Morphology of electrodes with PD0-1000 as active material a) before cycling and b) after 1000 cycles. Micromorphology of electrodes with PD5-1000 as active material c) before cycling and d) after 1000 cycles.

the reaction relaxation time. This suggests that morphology changes occurred in the electrode materials. Notably, the polymer-derived samples showed relatively large changes in EIS and charge transfer resistance, indicating that the active material experiences large capacity fluctuations at high current densities. The EIS fitting curves and results are provided in the Figure S7 and S8 and Table S2 (Supporting Information).

In order to further investigate the lithiation/de-lithiation mechanism of HESO anodes, in situ XRD was performed during charging–discharging for the first two cycles (**Figure 10**d). At the beginning of the first cycle, a significant shift of the reflection of the (311) plane of HESO to lower 2θ angles was observed, indicative of lattice expansion, which suggests that Li-ions embedded in the lattice of high-entropy spinel oxide at the beginning of the discharge. Meanwhile, the diffraction peaks of active material become broader, which is attributed to the embedded lithium ions expanding the grain volume and eventually breaking it, resulting in a smaller crystallite size. As the discharge proceeded, new diffraction peaks appeared at around 36.2° and 40.9°, which implies the formation of a rock-salt phase (the XRD pattern from 15 to 90° is given in Figure S9, Supporting Information), consistent with the literature on lithium-doped spinel oxides.[75] When a large amount of lithium cations were embedded, severe lattice distortions and charge imbalances occurred, ultimately leading to the phase transformation of the active material from a spinel to a rock-salt structure, corresponding to the second long plateau period (≈0.5 V). The CV test confirmed this phase transition during lithiation. Significant peaks from 0.47 to 0.01 V can be observed in the first cycle of all samples (Figure 10a–c), but failed to be detected in the second and third cycles, which is consistent with the disappearance of the spinel phase in the in situ XRD, that is, the transition of the spinel to the rock-salt phase is irreversible. This phase transformation provides a large capacity, and the irreversibility of the phase transformation is consistent with a large capacity fading after the first discharge. Phase transition will lead to further grain fragmentation, resulting in poorer conductivity of the active material and further capacity fading in subsequent cycles. During the first charging process, the reflection of the (111) plane of the rock-salt phase shifted from 36.9 to 37.1°, and the (200) plane shifted from 42.7 to 43.0°, indicating a decrease in the lattice parameter of the rock-salt phase. Meanwhile, broad peaks (≈1.5 V) in the CV curves of all samples were also detected, which correspond to the disembedding of lithium ions from $(Li_xCr_{0.6}Mn_{0.6}Fe_{0.6}Co_{0.6}Ni_{0.6})O_4$.

As expected, the reflection of the (200) crystal plane of the rock-salt phase shifted between 42.7 and 43.0° with discharge/charge in the second cycle, and the CV peaks appeared at ≈0.9 V and ≈0.5 V during discharging and were observed at ≈1.5 V during charging in the second and third cycles. Therefore, the embedding and disembedding of lithium ions in the lattice of the rock-salt phase is demonstrated to be the main mechanism for the charging and discharging of high-entropy spinel oxides as anode materials. Combined with in situ XRD and CV results, we propose the anode reactions during charge–discharge as follows

$$\text{First discharge: } M_3O_{4(\text{spinel})} + xLi^+ + xe^- \rightarrow Li_xM_3O_{4(\text{rock-salt})} \quad (1)$$

$$\text{Charge: } Li_xM_3O_{4(\text{rock-salt})} \rightarrow Li_{x-\delta}M_3O_{4(\text{rock-salt})} + \delta^+ + \delta e^- \quad (2)$$

$$\text{Discharge: } Li_{x-\delta}M_3O_{4(\text{rock-salt})} + \delta Li^+ + \delta e^- \rightarrow Li_xM_3O_{4(\text{rock-salt})} \quad (3)$$

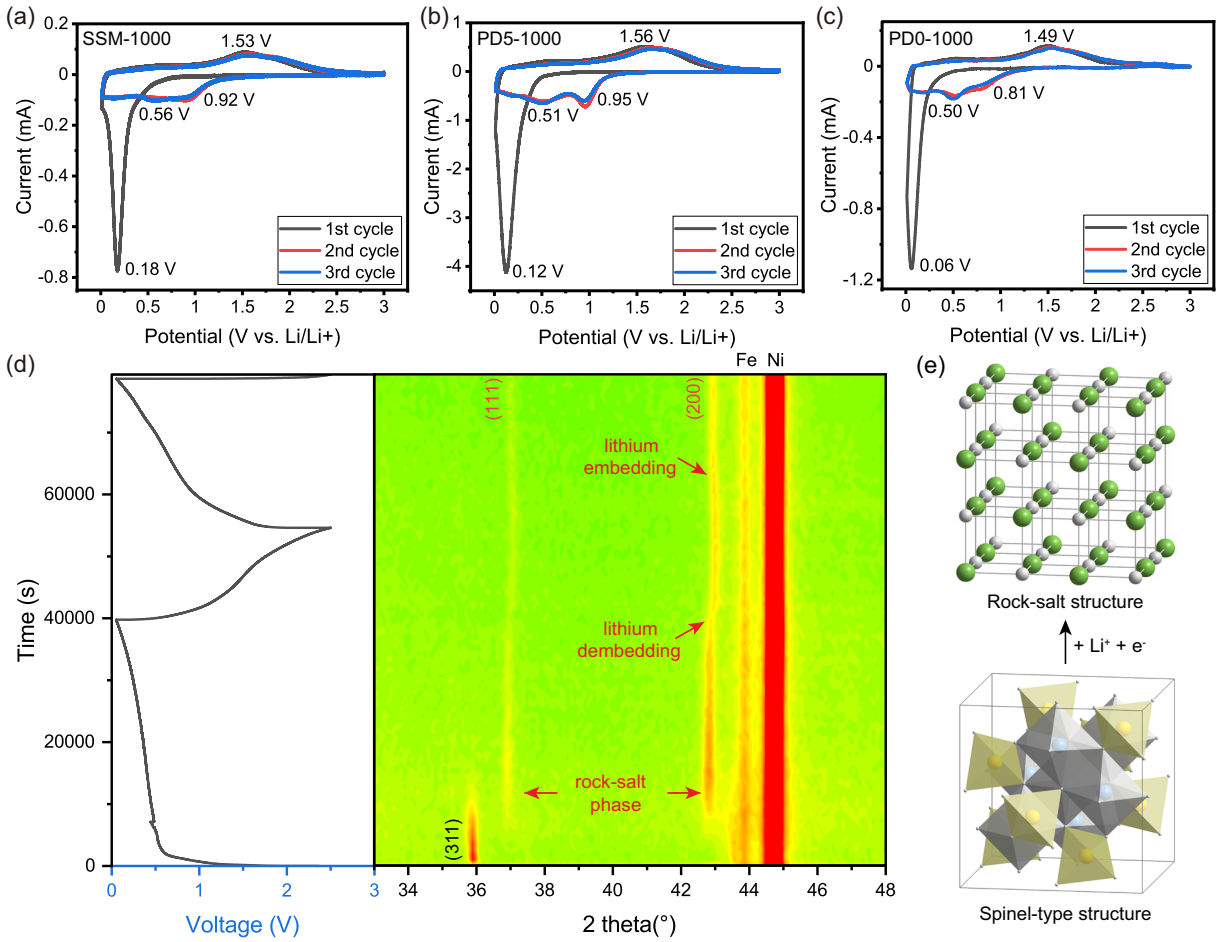

Figure 10. Cyclic voltammetry (CV) curves of a) SSM-1000, b) PD5-1000, and c) PD0-1000 at a scan rate of 0.1 mV s^{-1}. d) Charging—discharging in situ XRD of PD0-1000 in the first two cycles. The X-ray reflections at 43.9 and 44.7° correspond to the Fe shell of the cell and Ni foam, respectively. e) Illustration of the phase transformation during the first discharge. The yellow spheres represent the atoms in tetrahedral sites and the blue spheres represent the atoms in octahedral sites in the spinel-type structure. The green spheres represent Cr, Mn, Fe, Co, Ni, and Li in the rock-salt structure and the gray spheres represent oxygen.

Where the M represents transition metal elements, which are Cr, Mn, Fe, Co, and Ni in this work. M_3O_4 is the high-entropy spinel oxide, while $Li_xM_3O_4$ and $Li_{x-\delta}M_3O_4$ are the transformed rock-salt structural materials. The reflections of the (111) and (200) planes of the rock-salt phase were also observed in SSM-1000 (Figure S10, Supporting Information) and PD5-1000 (Figure S11, Supporting Information), and the shift of the (111) and (200) planes during subsequent charge–discharge was also observed, which suggest that the anodes composed of SSM-1000, PD5-1000, and PD0-1000 have the same electrochemical reactions during charge and discharge. The CV curves (Figure 10a–c) demonstrate that the electrochemical reaction potentials of the three anode materials from 0.01 to 3.0 V are basically the same. Compared to the in situ XRD patterns of PD0-1000, the reflection intensities of the secondary phase in SSM-1000 and PD5-1000 are considerably weaker. Particularly, the reflection of the (111) plane is too weak to distinguish in the second cycle, which is attributed to the severe grain fragmentation of SSM-1000 and PD5-1000 during cycling.

3. Conclusions

In this work, we successfully synthesized high-entropy spinel-type oxide by the modified Pechini process. Ex situ and in situ XRD demonstrated that the citric acid-assisted Pechini process effectively reduced the formation temperature of spinel-type high-entropy oxide to 600 °C, which is much lower than the formation temperatures observed for materials synthesized by the solid-state approach and wet chemistry method without chelation agent. The chelation and polyesterification reactions in the modified Pechini process lead to spatial retention of ions and homogeneous cation distribution, which reduce the ion diffusion distance and lead to lower formation temperatures of high-entropy ceramics. XAFS analysis and the Rietveld refinement of room-temperature neutron diffraction data determined the atomic occupancy of this spinel-type material, which is $(Mn_{0.05}Fe_{0.48}Co_{0.47}$, tetrahedral)$(Cr_{0.61}Mn_{0.52}Fe_{0.11}Co_{0.09}Ni_{0.68}$, octahedral)$O_4$. Materials prepared by Pechini and wet chemistry methods demonstrated large capacities as anodes for LIBs

compared to those synthesized by the solid-state method. However, the specimens synthesized by the Pechini method (i.e., with citric acid) showed a significant capacity fading, while the material obtained by the wet-chemistry method (i.e., without citric acid) exhibited minimal capacity fading at high current densities and maintained a capacity of ≈200 mAh g^{-1} after 1000 cycles. The generation of the rock-salt phase during cycling was detected for the first time by charging–discharging in situ XRD, and it is demonstrated that the charging–discharging of this anode material is achieved mainly through the embedding–disembedding of lithium ions in the lattice of the generated rock-salt phase. By reducing the grain size and avoiding grain fragmentation, the stability of high-entropy spinel oxides as anode materials is expected to be further improved, which will meet the requirements for energy storage in the future.

By comparing with literature data on the performance of spinel oxides as anodes for LIBs, we show that the capacity of spinel oxides as anodes for LIBs gradually increases with increasing number of cations, which is due to the synergistic effect of multiple metal cations with different reaction potentials and variable valence states in high-entropy materials.

4. Experimental Section

Synthesis of the Specimens: For the synthesis of multimetallic polymeric precursors, metal chlorides, $CrCl_3{\cdot}6H_2O$ (99.5%, Alfa Aesar), $MnCl_2{\cdot}6H_2O$ (99%, Chemsolute), $FeCl_3$ (98%, Alfa Aesar), $CoCl_2{\cdot}6H_2O$ (98%, Alfa Aesar), and $NiCl_2{\cdot}6H_2O$ (98%, Merck) were used as starting materials. Equimolar amount of 0.01 mol of all metal chlorides (i.e., 2.66 g $CrCl_3{\cdot}6H_2O$, 1.98 g $MnCl_2{\cdot}6H_2O$, 1.62 g $FeCl_3$, 2.38 g $CoCl_2{\cdot}6H_2O$, and 2.38 g $NiCl_2{\cdot}6H_2O$) were dissolved in 0.1 mol (5.59 mL) ethylene glycol (anhydrous, 99.8%, Sigma-Aldrich) in a flask, followed by stirring in a silicone oil bath at 80 °C for 30 min. After this step, the resulting solution was divided into two parts to investigate the effect of the chelation agent on the formation and structure of HESO. As a chelating agent, we use citric acid (anhydrous, 99.5%, Carl Roth), which was added in a molar ratio of 50% with respect to the total amount of metal cations, that is 0.025 mol (4.80 g) citric acid was added to the solution. In the next step, the samples were stirred at 110 °C for 1 h for the esterification and evaporation of the excess solvents. The precursors synthesized without citric acid were named PD0-PR and with citric acid were named PD5-PR. Both were thermally decomposed in air by heating to 400 °C for 1 h with a heating rate of 1°C min^{-1}. To investigate the required temperature for the formation of HESO, four different temperatures (600, 700, 800, and 1000 °C) were selected for the subsequent heat treatment in air. The specimens were heated to the required temperature with a heating rate of 1°C min^{-1}, held for 1 h, and then cooled to room temperature at a rate of 5°C min^{-1}. This treatment was done separately for each specimen (not in a consecutive way, i.e., not as 600 °C→700 °C→ 800 °C→ 1000 °C). A high-entropy spinel oxide of the same composition was synthesized also using a solid-state method. Binary oxides, Cr_2O_3 (1.52 g, 99%, Riedel-de Häen), MnO (1.42 g, 99%, Merck), Fe_2O_3 (1.60 g, 98%, Bayer), Co_2O_3 (1.66 g, 99%, Riedel-de Häen), and NiO (1.49 g, 99%, Riedel-de Häen), taken in a ratio to achieve the equimolar cations amount, were mixed by planetary ball milling (Retsch 183/81) with zirconia balls ($\varphi = 4$ mm) for 5 h in isopropanol. The mass ratio of the powder, zirconia balls, and isopropanol is about 1:3:1.2. The ball mill rested intermittently for 10 min every hour of milling and then restarted with the opposite direction of rotation. The solid-state mixture was obtained by drying the milled slurry in an oven at 70 °C for 10 h. Like the polymer-derived methods, the mixture was also calcined at different temperatures (i.e., 600, 700, 800, and 1000 °C) in the air for 1 h with a heating rate of 1 °C min^{-1}, then cooled to room temperature at a rate of 5 °C min^{-1}.

Characterization Methods: The composition and structure of the synthesized polymeric precursor (PD0-PR and PD5-PR) were elucidated by Fourier transform infrared spectroscopy (FTIR, Bruker VERTEX 70, Germany) in attenuated total reflection mode from 4000 to 550 cm^{-1}. The thermal decomposition processes of PD0-PR and PD5-PR were investigated by simultaneous thermal analysis (Netzsch STA 409 PC LUXX, Germany) coupled with mass spectrometry (OMNiStar GSD 320, Germany) from room temperature to 800 °C with a heating rate of 10 °C min^{-1} in air. The metal element content was determined by ICP-OES in a Horiba Scientific ICP Ultima2 (Horiba, Japan). Powder samples were digested in an aqueous suspension of HNO_3 at 200 °C for 5 h in an autoclave. The phase compositions of materials calcined at 600, 700, 800, and 1000 °C for 1 h were examined by XRD (Bruker D8 Advance Diffractometer, USA) with reflection mode using Cu-Kα radiation ($\lambda = 1.5406$ Å). The calcined samples were ground to a fine powder and flattened on a single crystal silicon sample holder for the measurement. 2θ value ranging from 15 to 90°, with step size and time of 0.01° and 0.2 s, respectively. In situ high-temperature synchrotron XRD experiments were performed at the beamline P02.1, PETRA III electron storage ring (Deutsches Elektronen-Synchrotron, DESY, Hamburg) with a wavelength of 0.20735 Å. Since the organic components in the polymer-derived samples can be completely decomposed at 400 °C, PD0-PR and PD5-PR were preheat-treated in air at 400 °C for 1 h before measurement. One to two milligrams of sample powder are loaded in between silica wool beds inside an amorphous quartz capillary of 1 mm internal diameter (Hilgenberg, Germany) and heated under a continuous synthesized air flow (10 mL min^{-1}) at a rate of 10 °C min^{-1} to 1000 °C in an infrared-heated SiC tube furnace as described elsewhere.[54] Diffraction patterns were recorded by a Varex XRD 4343CT detector (150 × 150 μm^2 pixel size), with 60 s acquisition time, utilizing a 0.5 × 0.5 mm^2 beam size. The sample-detector distance and instrumental peak broadening were calibrated with a LaB_6 (NIST 660b) standard. The 2D images were integrated using Dioptas.[55] To allow sufficient diffusion of the materials after the in situ XRD measurement, samples were held for 10 min at 1000 °C and recorded diffractograms, which were used for Rietveld refinements. Neutron-diffraction measurements were performed on the high-resolution two-axis diffractometer D2B at the Institut Laue Langevin (ILL, Grenoble, France). The diffractograms were recorded with a wavelength of $\lambda = 1.5940$ Å at room temperature. Rietveld refinement analysis of XRD and neutron data was performed using FullProf Suite software.[56]

The morphology of the calcined powders and the prepared electrolyte were examined by SEM (LEO Gemini 1530, Carl, Zeiss, Germany) with an in-lens detector. The calcined samples were ground into fine powder and adhered to carbon tapes on aluminum sample stages. Electrodes were removed from the cells and washed with dimethyl carbonate and ethanol, followed by being adhered to the carbon tapes on the sample stages for the test. All the samples were not sputter coated. EDS (Thermo Fisher Scientific Inc., USA) mapping was further used to measure elemental content and spatial distribution. TEM was conducted to evaluate the crystal structure, morphology, and elemental distribution of the nanoparticles. TEM brightfield images, HR-TEM images, and diffraction patterns were acquired using a conventional Tecnai $G^2$20 S-TWIN (FEI/TFS company, USA) with LaB_6 electron source, operated at 200 kV. To determine the elemental distribution, EDS-mappings were collected using a probe-Cs corrected JEM-ARM300F2 STEM instrument (JEOL Ltd., Japan) with cold FEG electron source, operated at 80 kV. The instrument is equipped with a dual SDD EDS system (JEOL Ltd., Japan) providing a large detection angle of 2.2 sr. Lowering the acceleration voltage to 80 kV suppresses instrument-related peaks, detectable in the EDS spectrum, but some of such peaks remain. Therefore, Au, Al, Cu, Si, and Ti are not present in the sample but are detectable from inside the microscope, caused by scattering events. Due to the ferromagnetic properties of the material, the preparation of the samples for TEM required additional precautions. A small amount of the powder was dispersed in ethanol by ultrasonication for 1 min. The dispersion was then settled with the help of a strong NdFe magnet, to filter large particles out, because they can potentially harm the electron microscopes. Three microliters of the filtered dispersion was then

drop-casted to 300 mesh holey carbon Cu grids. The grids were dried at 40 °C in air.

XAFS measurements for the K-edges of Cr, Mn, Fe, Co, and Ni were carried out with a self-developed wavelength-dispersive spectrometer in von Hámos geometry.[57,58] The spectrometer is equipped with a microfocus X-Ray tube with molybdenum as anode material, a curved highly annealed pyrolytic graphite mosaic crystal, and a hybrid photon counting CMOS detector with 512 × 1030 pixel and a pixel size of 75 × 75 μm. The tube was operated with a high voltage of 11 kV and a current of 1440 μA for the Cr-K edge with the lowest energy and with 15.5 kV and a current of 1910 μA for the Ni-K edge with the highest energy. The sample was prepared with Hoechst Wax as a pellet with a pellet diameter of 13 mm. The reference materials were either prepared as a Hoechst wax pellet or the powder was directly applied on an adhesive tape. The samples and references were measured in transmission and were constantly moved during the measurements to minimize the effects of local thickness inhomogeneity. For the normalization of the data and further analysis of the spectra, ATHENA of the Demeter software package has been used.[59] Due to the lack of suitable reference materials, synchrotron spectra measured on BL14B2 at SPring-8 were used, which were published in the Materials Data Repository.[60,61] To compare laboratory data with synchrotron spectra, laboratory data of the metal foils and powder were aligned with data from the SPring-8. The FT-EXAFS of the spectra was done with the ATHENA software with the following parameters: spline range in k: 0–10, the range for the Forward Fourier transformation: 3 to 9 with a dk of 1, the Hanning window function, and a plotting k-weight of 2.

Electrochemical Characterization: Cell Assembly: Coin cells were assembled to test the electrochemical performance of synthesized HESO as anode active materials as shown in the following steps. To compare the impact of processing parameters, SSM-800, SSM-1000, PD0-800, PD0-1000, PD5-800, and PD5-1000 were respectively used as the active materials of anodes. The active materials were ground by hand milling into a fine powder (80 wt%) and then mixed with 10 wt% sodium carboxymethyl cellulose (92%, Sigma-Aldrich) in an aqueous solution (0.1 g in 40 mL of water) and 10 wt% conductive carbon black (99%, Timcal) to form a uniform slurry. Then, the slurry was cast on the rough surface of the copper foil, and the prepared electrode was dried in a vacuum oven at 80 °C for 20 h to remove the solvent. After drying, the electrode with a diameter of 12 mm was punched out and pressed with a press machine under 3 kN for 2 min. Then, electrodes were dried at room temperature for 12 h and transferred to an Ar-filled glove box (H_2O and $O_2 < 0.1$ ppm). Coin cells were assembled in an Ar-filled glove box. Metallic Li pressed on a steel sheet and served as a counter electrode separated by a glass fiber filter as separator, imbibed by lithium hexafluorophosphate ($LiPF_6$, 1 M $LiPF_6$ in ethylene carbonate: dimethyl carbonate=50:50, Sigma–Aldrich) solution as the electrolyte. Spring was added to provide pressure and the whole coin cell was covered by a CR2032 stainless steel button.

Electrochemical Characterization: The assembled coin cells were connected to a source meter unit (Yokogawa GS610 and KEI2: Keithley 2400) to investigate electrochemical properties. The units were controlled with a self-written LabVIEW program. The potential range was 0.05 to 2.5 V (V versus Li/Li+). The battery was formed under a current density of 37 mA g^{-1} for 3 cycles. The rate performance was tested by the following current densities sequence: 74, 185, 370, 740, 1850, and 74 mA g^{-1} (i.e., 0.2, 0.5, 1, 2, 5, and 0.2 times of 370 mA g^{-1}) for 5 cycles, respectively. The system rested 6 s after each charge and discharge. The cycling performance was conducted on the cells after formation at a current density of 1 A g^{-1} for 1000 cycles. The pulsed discharge/charge test coupled with EIS measurements was conducted on coin cells after 10 cycles and 1000 cycles at a current density of 500 mA g^{-1}. This measurement was conducted with a Zahner Im6ex workstation in potentiostatic mode with 5 mV amplitude between 50 MHz and 1 MHz. The test program was programmed with the Zahner software tool "Script" (based on BASIC). The cell was discharged to 0.05 V and charged to 2.5 V at a current density of 74 mA g^{-1}. The charging was stopped at several potentials (25, 50, and 75%) of the state of charge (SoC) and relaxed for several hours (2, 2, 2, 0.5, 1, 2, and 4 h) followed by EIS measurement. Cyclic voltammetry measurement was also performed on a Zahner Im6ex workstation within a range of 0.01–3.0 V (versus Li/Li^+) with a potential sweep rate of 0.1 mV s^{-1}.

Electrochemical Characterization: Operando X-Ray Diffraction: Charging–discharging operando XRD characterization was conducted in a homemade cell as described in our previous work.[11] A stainless coin-type cell (10 mm window in the center of the positive can that is covered with copper-coated Kapton foil) was used for in situ XRD measurements. SSM-1000, PD5-1000, and PD0-1000 were used as active materials to prepare the slurry as described in the cell assembly part above, followed by casting on a nickel foam (100 ppi, porosity 98%, thickness 0.3 mm) with a diameter of 12 mm. The prepared cell was cycled in the voltage range of 0.05–2.5 V at a current density of 185 mA g^{-1}. The XRD patterns were collected on the same equipment mentioned above, from 33 to 48° with step size and time of 0.02° and 1 s.

Supporting Information

Supporting Information is available from the Wiley Online Library or from the author.

Acknowledgements

This work was supported by the China Scholarship Council (201907565035). The authors would like to acknowledge Huaiyou Chen for the FTIR analysis, Harald Link for the ICP-OES analysis, Sara Santos for the SEM and EDS measurements, and Dr. Wolfgang Brehm for the cycling test, all from Technische Universität Berlin. The authors thank Sören Selve from Zentraleinrichtung Elektronenmikroskopie (ZELMI) at Technische Universität Berlin for TEM support and the German Research Foundation (DFG) for funding within the project 403371556—GZ: INST 131/789-1 FUGG. The authors are grateful to Delta Materials GmbH for providing nickel foams. The authors also acknowledge Martin Etter, Henrik S. Jeppesen, and DESY (Hamburg, Germany), a member of the Helmholtz Association HGF, for the provision of experimental facilities. Parts of this research were carried out at PETRA III, beamline P02.1, under proposal ID (LTP II-20210010).

Conflict of Interest

The authors declare no conflict of interest.

Author Contributions

Haotian Yang: Conceptualization (lead); Data curation (lead); Formal analysis (lead); Investigation (lead); Methodology (lead); Writing—original draft (lead). **Ge Chen**: Data curation (equal); Formal analysis (supporting); Investigation (supporting); Methodology (equal). **Jiaqi Ni**: Data curation (equal); Formal analysis (supporting); Investigation (equal); Writing—original draft (supporting). **Sebastian Praetz**: Data curation (equal); Formal analysis (supporting); Investigation (equal). **Delf Kober**: Methodology (equal). **Gabriel Cuello**: Investigation (supporting). **Emiliano Dal Molin**: Investigation (supporting). **Albert Gili**: Investigation (supporting). **Christopher Schlesiger**: Investigation (supporting). **Maged F. Bekheet**: Data curation (supporting); Formal analysis (supporting); Investigation (supporting); Writing—review and editing (equal). **Dorian A. H. Hanaor**: Conceptualization (supporting); Project administration (equal); Supervision (equal); Writing—review and editing (equal). **Aleksander Gurlo**: Conceptualization (supporting); Resources (lead); Supervision (equal); Writing—review and editing (equal).

Data Availability Statement

The data that support the findings of this study are available in the supplementary material of this article.

Keywords

high-entropy materials, in situ X-ray diffraction, Li-ion batteries, Pechini process

Received: May 15, 2024
Revised: August 29, 2024
Published online: September 19, 2024

[1] B. Ran, H. Li, R. Cheng, Z. Yang, Y. Zhong, Y. Qin, C. Yang, C. Fu, *Adv. Sci.* **2024**, *11*, 2401034.
[2] A. Eftekhari, Z. Jian, X. Ji, *ACS Appl. Mater. Interfaces* **2017**, *9*, 4404.
[3] W. Guo, J. Wang, A. Gurlo, M. F. Bekheet, *Batteries Supercaps* **2024**, *7*, e202400032.
[4] W. Guo, O. Icin, C. Vakifahmetoglu, D. Kober, A. Gurlo, M. F. Bekheet, *Adv. Funct. Mater.* **2023**, *33*, 2304933.
[5] W. Guo, D. A. H. Hanaor, D. Kober, J. Wang, M. F. Bekheet, A. Gurlo, *Batteries* **2022**, *8*, 116.
[6] Y. Fu, X. Pei, Y. Dai, D. Mo, S. Lyu, *ES Energy Environ.* **2019**, *4*, 66.
[7] Y. Yao, J. Zheng, Z. Gong, Z. Ding, J. Zhang, W. Yu, D. M. Bengono, H. Li, B. Zhang, H. Tong, *J. Alloys Compd.* **2019**, *790*, 288.
[8] X. Zhang, X. Li, F. Jiang, W. Du, C. Hou, Z. Xu, L. Zhu, Z. Wang, H. Liu, W. Zhou, H. Yuan, *Dalton Trans.* **2020**, *49*, 1794.
[9] S. Zavareh, A. Hilger, K. Hirselandt, O. Goerke, I. Manke, J. Banhart, A. Gurlo, *J. Ceram. Soc. Jpn.* **2016**, *124*, 1067.
[10] G. Shao, D. A. H. Hanaor, J. Wang, D. Kober, S. Li, X. Wang, X. Shen, M. F. Bekheet, A. Gurlo, *ACS Appl. Mater. Interfaces* **2020**, *12*, 46045.
[11] J. Wang, D. Kober, G. Shao, J. D. Epping, O. Görke, S. Li, A. Gurlo, M. F. Bekheet, *Mater. Today Energy* **2022**, *26*, 100989.
[12] T. D. Sparks, A. Gurlo, M. F. Bekheet, M. W. Gaultois, G. Cherkashinin, L. Laversenne, D. R. Clarke, *Phys. Rev. B* **2019**, *99*, 104104.
[13] M. F. Bekheet, L. Schlicker, A. Doran, K. Siemensmeyer, A. Gurlo, *Dalton Trans.* **2018**, *47*, 2727.
[14] D. Chen, G. Ji, Y. Ma, J. Y. Lee, J. Lu, *ACS Appl. Mater. Interfaces* **2011**, *3*, 3078.
[15] G. Zhou, D.-W. Wang, F. Li, L. Zhang, N. Li, Z.-S. Wu, L. Wen, G. Q. Lu, H.-M. Cheng, *Chem. Mater.* **2010**, *22*, 5306.
[16] T. Kozawa, F. Kitabayashi, K. Fukuyama, M. Naito, *Sci. Rep.* **2022**, *12*, 11992.
[17] H. Wang, L.-F. Cui, Y. Yang, H. Sanchez Casalongue, J. T. Robinson, Y. Liang, Y. Cui, H. Dai, *J. Am. Chem. Soc.* **2010**, *132*, 13978.
[18] Z.-S. Wu, W. Ren, L. Wen, L. Gao, J. Zhao, Z. Chen, G. Zhou, F. Li, H.-M. Cheng, *ACS Nano* **2010**, *4*, 3187.
[19] J. Liu, H. Xia, L. Lu, D. Xue, *J. Mater. Chem.* **2010**, *20*, 1506.
[20] X. Zhu, G. Ning, X. Ma, Z. Fan, C. Xu, J. Gao, C. Xu, F. Wei, *J. Mater. Chem. A* **2013**, *1*, 14023.
[21] L. Wang, Y. Zheng, X. Wang, S. Chen, F. Xu, L. Zuo, J. Wu, L. Sun, Z. Li, H. Hou, Y. Song, *ACS Appl. Mater. Interfaces* **2014**, *6*, 7117.
[22] N. Qiu, H. Chen, Z. Yang, S. Sun, Y. Wang, Y. Cui, *J. Alloys Compd.* **2019**, *777*, 767.
[23] N. Yan, L. Hu, Y. Li, Y. Wang, H. Zhong, X. Hu, X. Kong, Q. Chen, *J. Phys. Chem. C* **2012**, *116*, 7227.
[24] X. Yan, L. Constantin, Y. Lu, J.-F. Silvain, M. Nastasi, B. Cui, *J. Am. Ceram. Soc.* **2018**, *101*, 4486.
[25] B. Ye, T. Wen, K. Huang, C.-Z. Wang, Y. Chu, *J. Am. Ceram. Soc.* **2019**, *102*, 4344.
[26] J. Zhou, J. Zhang, F. Zhang, B. Niu, L. Lei, W. Wang, *Ceram. Int.* **2018**, *44*, 22014.
[27] J. X. Yang, B.-H. Dai, C.-Y. Chiang, I.-C. Chiu, C.-W. Pao, S.-Y. Lu, I.-Y. Tsao, S.-T. Lin, C.-T. Chiu, J.-W. Yeh, P.-C. Chang, W.-H. Hung, *ACS Nano* **2021**, *15*, 12324.
[28] H. Chen, K. Jie, C. J. Jafta, Z. Yang, S. Yao, M. Liu, Z. Zhang, J. Liu, M. Chi, J. Fu, S. Dai, *Appl. Catal. B Environ.* **2020**, *276*, 119155.
[29] X. Han, V. Girman, R. Sedlak, J. Dusza, E. G. Castle, Y. Wang, M. Reece, C. Zhang, *J. Eur. Ceram. Soc* **2020**, *40*, 2709.
[30] R. Liu, H. Chen, K. Zhao, Y. Qin, B. Jiang, T. Zhang, G. Sha, X. Shi, C. Uher, W. Zhang, L. Chen, *Adv. Mater.* **2017**, *29*, 1702712.
[31] A. Sarkar, L. Velasco, Q. Di Wang, *Nat. Commun.* **2018**, *9*, 3400.
[32] Q. Wang, A. Sarkar, L. Di Wang, *Energy Environ. Sci.* **2019**, *12*, 2433.
[33] D. Wang, S. Jiang, C. Duan, J. Mao, Y. Dong, K. Dong, Z. Wang, S. Luo, Y. Liu, X. Qi, *J. Alloys Compd.* **2020**, *844*, 156158.
[34] R.-Z. Zhang, M. J. Reece, *J. Mater. Chem. A* **2019**, *7*, 22148.
[35] Y. Han, X. Liu, Q. Zhang, M. Huang, Y. Li, W. Pan, P.-A. Zong, L. Li, Z. Yang, Y. Feng, P. Zhang, C. Wan, *Nat. Commun.* **2022**, *13*, 2871.
[36] W.-Z. Li, L. Kovarik, D. Mei, J. Liu, Y. Wang, C. H. F. Peden, *Nat. Commun.* **2013**, *4*, 2481.
[37] J. O. Olowoyo, R. J. Kriek, *Small* **2022**, *18*, e2203125.
[38] B. Musicó, Q. Wright, T. Z. Ward, A. Grutter, E. Arenholz, D. Gilbert, D. Mandrus, V. Keppens, *Phys. Rev. Mater.* **2019**, *3*, 104416.
[39] B. Xiao, G. Wu, T. Wang, Z. Wei, Y. Sui, B. Shen, J. Qi, F. Wei, J. Zheng, *Nano Energy* **2022**, *95*, 106962.
[40] W. Hooch Antink, S. Lee, H. S. Lee, H. Shin, T. Y. Yoo, W. Ko, J. Shim, G. Na, Y.-E. Sung, T. Hyeon, *Adv. Funct. Mater.* **2024**, *34*, 2309438.
[41] R. R. Katzbaer, F. M. Dos Santos Vieira, I. Dabo, Z. Mao, R. E. Schaak, *J. Am. Chem. Soc.* **2023**, *145*, 6753.
[42] J. Dąbrowa, M. Stygar, A. Mikuła, A. Knapik, K. Mroczka, W. Tejchman, M. Danielewski, M. Martin, *Mater. Lett.* **2018**, *216*, 32.
[43] Z. Jin, J. Lyu, Y.-L. Zhao, H. Li, X. Lin, G. Xie, X. Liu, J.-J. Kai, H.-J. Qiu, *ACS Mater. Lett.* **2020**, *2*, 1698.
[44] X.-F. Luo, J. Patra, W.-T. Chuang, T. X. Nguyen, J.-M. Ting, J. Li, C.-W. Pao, J.-K. Chang, *Adv. Sci.* **2022**, *9*, e2201219.
[45] T. X. Nguyen, C.-C. Tsai, J. Patra, O. Clemens, J.-K. Chang, J.-M. Ting, *Chem. Eng. J.* **2022**, *430*, 132658.
[46] C. Triolo, M. Maisuradze, M. Li, Y. Liu, A. Ponti, G. Pagot, V. Di Noto, G. Aquilanti, N. Pinna, M. Giorgetti, S. Santangelo, *Small* **2023**, *19*, e2304585.
[47] S. Hou, L. Su, S. Wang, Y. Cui, J. Cao, H. Min, J. Bao, Y. Shen, Q. Zhang, Z. Sun, C. Zhu, J. Chen, Q. Zhang, F. Xu, *Adv. Funct. Mater.* **2024**, *34*, 2307923.
[48] S. Goriparti, E. Miele, F. de Angelis, E. Di Fabrizio, R. Proietti Zaccaria, C. Capiglia, *J. Power Sources* **2014**, *257*, 421.
[49] M. Xu, Q. Xia, J. Yue, X. Zhu, Q. Guo, J. Zhu, H. Xia, *Adv. Funct. Mater.* **2019**, *29*, 1807377.
[50] F. Kamutzki, M. F. Bekheet, S. Schneider, A. Gurlo, D. A. Hanaor, *Open Ceram.* **2022**, *9*, 100241.
[51] W.-F. Chen, S. S. Mofarah, D. A. H. Hanaor, P. Koshy, H.-K. Chen, Y. Jiang, C. C. Sorrell, *Inorg. Chem.* **2018**, *57*, 7279.
[52] F. Kamutzki, S. Schneider, J. T. Müller, J. Barowski, D. Klimm, A. Gurlo, D. A. H. Hanaor, *Phys. Status Solidi A* **2023**, *220*, 2200685.
[53] H. Yang, S. Klemm, J. Müller, M. F. Bakheet, A. Gurlo, D. A. Hanaor, *J. Eur. Ceram. Soc.* **2023**, *43*, 4233.
[54] B. Bischoff, M. F. Bekheet, E. Dal Molin, S. Praetz, B. Kanngießer, R. Schomäcker, M. Etter, H. S. Jeppesen, A. Tayal, A. Gurlo, A. Gili, *J. Synchrotron. Rad.* **2024**, *31*, 77.
[55] C. Prescher, V. B. Prakapenka, *High Pressure Res.* **2015**, *35*, 223.
[56] J. Rodriguez-Carvajal, *Newsletter* **2001**, *26*, 12.

[57] C. Schlesiger, L. Anklamm, H. Stiel, W. Malzer, B. Kanngießer, *J. Anal. Atom. Spectrom.* **2015**, *30*, 1080.
[58] C. Schlesiger, S. Praetz, R. Gnewkow, W. Malzer, B. Kanngießer, *J. Anal. Atom. Spectrom.* **2020**, *35*, 2298.
[59] B. Ravel, M. Newville, *J. Synchrotron. Rad.* **2005**, *12*, 537.
[60] M. Ishii, H. Nagao, K. Tanabe, A. Matsuda, H. Yoshikawa, *MDR XAFS DB. Materials Data Repository*, National Institute for Materials Science, https://doi.org/10.48505/nims.1447.
[61] M. Ishii, K. Tanabe, A. Matsuda, H. Ofuchi, T. Matsumoto, T. Yaji, Y. Inada, H. Nitani, M. Kimura, K. Asakura, *Sci. Technol. Adv. Mater. Methods* **2023**, *3*, 2197518.
[62] X. Ma, W. Zhong, J. Zhao, S. L. Suib, Y. Lei, *Eng. Sci.* **2020**, *9*, 99.
[63] B. L. Mojet, S. D. Ebbesen, L. Lefferts, *Chem. Soc. Rev.* **2010**, *39*, 4643.
[64] M. Burgos, M. Langlet, *Thin Solid Films* **1999**, *349*, 19.
[65] C. Yan, R. Liu, Y. Cao, C. Zhang, D. Zhang, *J. Sol.-Gel Sci. Technol.* **2012**, *64*, 251.
[66] F. M. Courtel, H. Duncan, Y. Abu-Lebdeh, I. J. Davidson, *J. Mater. Chem.* **2011**, *21*, 10206.
[67] J. Wang, N. Yang, H. Tang, Z. Dong, Q. Jin, M. Yang, D. Kisailus, H. Zhao, Z. Tang, D. Wang, *Angew. Chem. Int. Ed. Engl.* **2013**, *52*, 6417.
[68] M. V. Reddy, C. Y. Quan, K. W. Teo, L. J. Ho, B. V. R. Chowdari, *J. Phys. Chem. C* **2015**, *119*, 4709.
[69] M. V. Reddy, C. Yao Quan, S. Adams, *Mater. Lett.* **2018**, *212*, 186.
[70] L. Li, Q. Yao, J. Liu, K. Ye, B. Liu, Z. Liu, H. Yang, Z. Chen, J. Duan, B. Zhang, *Front. Chem.* **2018**, *6*, 153.
[71] M. Bijelić, X. Liu, Q. Sun, A. B. Djurišić, M. H. Xie, A. M. C. Ng, C. Suchomski, I. Djerdj, Ž. Skoko, J. Popović, *J. Mater. Chem. A* **2015**, *3*, 14759.
[72] J. Patra, T. X. Nguyen, C.-C. Tsai, O. Clemens, J. Li, P. Pal, W. K. Chan, C.-H. Lee, H.-Y. T. Chen, J.-M. Ting, J.-K. Chang, *Adv. Funct. Mater.* **2022**, *32*, 2110992.
[73] B. Xiao, G. Wu, T. Wang, Z. Wei, Z. Xie, Y. Sui, J. Qi, F. Wei, X. Zhang, L.-B. Tang, J.-C. Zheng, *ACS Appl. Mater. Interfaces* **2023**, *15*, 2792.
[74] J. Cabana, L. Monconduit, D. Larcher, M. R. Palacín, *Adv. Mater.* **2010**, *22*, E170.
[75] J. Wang, D. Stenzel, R. Azmi, S. Najib, K. Wang, J. Jeong, A. Sarkar, Q. Wang, P. A. Sukkurji, T. Bergfeldt, M. Botros, J. Maibach, H. Hahn, T. Brezesinski, B. Breitung, *Electrochem* **2020**, *1*, 60.